The Astrophysical Journal, 890:107 (14pp), 2020 February 20 https://doi.org/10.3847/1538-4357/ab68e4
© 2020. The American Astronomical Society. All rights reserved.

Internal Structure and CO_2 Reservoirs of Habitable Water Worlds

Nadejda Marounina and Leslie A. Rogers
Department of Astronomy and Astrophysics, University of Chicago, Chicago, IL 60637, USA; nmarounina@gmail.com
Received 2018 October 1; revised 2020 January 3; accepted 2020 January 6; published 2020 February 18

Abstract

Water worlds are water-rich (>1 wt% H_2O) exoplanets. The classical models of water worlds considered layered structures determined by the phase boundaries of pure water. However, water worlds are likely to possess comet-like compositions, with between ∼3 and 30 mol% CO_2 relative to water. In this study, we build an interior structure model of habitable (i.e., surface liquid ocean–bearing) water worlds using the latest results from experimental data on the CO_2–H_2O system to explore the CO_2 budget and localize the main CO_2 reservoirs inside of these planets. We show that CO_2 dissolved in the ocean and trapped inside of a clathrate layer cannot accommodate a cometary amount of CO_2 if the planet accretes more than 11 wt% of volatiles ($CO_2 + H_2O$) during its formation. If the atmosphere holds more than a negligible amount of the CO_2 (>0.01% of the planet mass), the planet will not have a habitable surface temperature. We propose a new, potentially dominant, CO_2 reservoir for water worlds: CO_2 buried inside of the high-pressure water ice mantle as CO_2 ices or ($H_2CO_3 \cdot H_2O$), the monohydrate of carbonic acid. If insufficient amounts of CO_2 are sequestered in either this reservoir or the planet's iron core, habitable-zone water worlds could generically be stalled in their cooling before liquid oceans have a chance to condense.

Unified Astronomy Thesaurus concepts: Planetary interior (1248); Ocean planets (1151); Carbon dioxide (196); Habitable planets (695); Exoplanets (498); Ocean-atmosphere interactions (1150); Hydrosphere (770)

1. Introduction

Water-rich exoplanets (>1% water by mass) will be the next accessible targets on the path of the observation of Earth-like planets (e.g., Beichman et al. 2014). Water-rich planets possess lower densities and larger radii than terrestrial Earth-like planets with similar masses, making them more amenable to observations and characterization by future surveys. Kuchner (2003) and Léger et al. (2004) were the first to propose the existence of water-rich planets, suggesting that they would form beyond the snow line and accrete comet-like proportions of rocky material and ices. Then, interactions with protoplanetary disks or other bodies in the system would bring them into the habitable zone (HZ) of their star, forming a global water ocean at their surfaces. Since then, Luger et al. (2015) has shown that photoevaporation of an H_2/He envelope from a mini-Neptune could be another path of formation of water worlds, especially relevant for planets in the HZs of M dwarfs. Additionally, several theoretical studies predict an efficient accretion of volatiles during planet assembly (especially in scenarios with low-mass host stars and long-lived protoplanetary disks), forming planets with up to ∼50% of water by mass (Raymond et al. 2004; Alibert & Benz 2017; Kite & Ford 2018). Thus, water-rich planets are possibly numerous around M dwarfs and will be prime targets for atmospheric characterization in the near future. Indeed, the recent discovery and characterization of the TRAPPIST-1 system has shown that it may contain HZ planets with several tens of percent of water by mass (Gillon et al. 2017; Grimm et al. 2018; Unterborn et al. 2018a, 2018b).

At the present time, a widely accepted terminology for the denomination of water-rich exoplanets does not exist, and terms such as "water world" or "ocean planet" may have different meanings from paper to paper. Here we choose to call a "water world" any planet with sufficient quantities of volatiles that it could form a high-pressure water ice layer given a favorable interior temperature profile (regardless of whether the planet actually cools sufficiently for the high-pressure ice to form). By this definition, a water world could have a subsurface ocean, a surface global or partial ocean, or, in the most extremes cases, no ocean at all, with the volatile-rich envelope entirely in a supercritical or vapor state.

The common definition of the HZ does not apply to water worlds, and the habitability of water worlds is still poorly constrained. Computations of the HZs mostly focus on the Earth-like planets, where continent and seafloor weathering stabilizes the concentration of CO_2 in the atmosphere, inducing a negative feedback (e.g., Walker et al. 1981; Kasting et al. 1993; Kasting & Catling 2003; Kopparapu et al. 2013). Such feedback is probably not active for habitable water worlds or water worlds with global surface water oceans because silicates are likely to be isolated from liquid water by a high-pressure ice mantle (Léger et al. 2004; Sotin & Grasset 2007; Fu et al. 2010; Levi et al. 2013, 2017). Assuming that the high-pressure ice layer precludes chemical exchanges between the silicate layers and liquid water, the partial pressure of CO_2 in the atmosphere would be controlled by the total amount of CO_2 in the hydrosphere (i.e., volatile-dominated layers of the planet) and the temperature profile inside of these volatile-rich layers.

Water worlds are likely to possess CO_2-rich bulk compositions. Kuchner (2003), Léger et al. (2004), and Selsis et al. (2007) proposed that water worlds would initially form with comet-like compositions. In comets, CO_2 is the second most abundant volatile after H_2O, ranging from ∼3 to 30 mol% relative to water (e.g., Bockelee-Morvan et al. 2004; Mumma & Charnley 2011; Ootsubo et al. 2012). For these planets, the pressure at the ice–silicate interface exceeds the limiting pressure for volcanic degassing (∼0.6 GPa; Kite et al. 2009). Therefore, CO_2 is not supplied to the hydrosphere by volcanism from the silicate layers of the planet, and the total CO_2 mass in the hydrosphere does not vary substantially after the planet forms and differentiates.

In the scenario where water worlds form by photoevaporation (Luger et al. 2015), the amount of CO_2 left in the planet's atmosphere would depend on the overall CO_2 accretion and escape history. Luger et al. (2015) proposed that planets that have lost their hydrogen envelopes may still possess high-density atmospheres with considerable amounts of CO_2.

Only a small fraction of the CO_2 accreted by a water world can reside in the planet's atmosphere if the water world is to maintain a temperate surface temperature and a surface liquid water ocean. Indeed, even the highest CO_2 partial pressures allowed inside of the HZ ($P_{CO_2} \sim 100$ bars; Figure 6) correspond to less than 1 wt% CO_2 relative to the total volatile content of the planet. Depending on the orbital separation of the planet, the host star, and the planet history, higher amounts of CO_2 in the atmosphere could lead either to (i) the evaporation of the liquid oceans or (ii) the prevention of liquid oceans from condensing in the first place, as the planet is impeded from cooling from its postaccretion hot state. To avoid this situation, much of the CO_2 accreted by the planet would need to be sequestered in the planetary interior, separate from the atmosphere, because CO_2 reservoirs in contact with the atmosphere could be easily destabilized by temperature changes (Kitzmann et al. 2015; Levi et al. 2017).

The water-dominated layers of the hydrosphere can store only a limited amount of CO_2. If these layers are saturated, the excess of carbon dioxide will form a new, separate phase. To set an upper limit on the amount of CO_2 that can be stored in these water-rich layers, here we consider the extreme scenario in which they are fully saturated. Therefore, in the rest of this work, we distinguish between CO_2-saturated reservoirs (which designate the storage of CO_2 by saturating water-dominated layers) and excess CO_2 reservoirs (i.e., CO_2 reservoirs that would form if water-dominated layers are saturated). One example of a saturated reservoir would be the water ocean, while an example of an excess reservoir is the atmosphere.

Previous work on water-rich exoplanets explored the potential interactions between the ocean and the atmosphere in great detail but did not examine how/if the overall CO_2 budget and the distribution of CO_2 throughout the hydrosphere would even allow the presence of liquid water at the surface of water worlds. Kitzmann et al. (2015) was the first to compute the HZ of water worlds possessing liquid water oceans at their surfaces. The study constrains the size of the HZ for a range of partial pressures of CO_2. It also points out that a solubility-controlled CO_2 abundance in the atmosphere constitutes an unstable CO_2 feedback cycle, and any perturbation in temperature or atmospheric CO_2 content could lead to a runaway greenhouse or the freezing of the surface. The extensive study of Levi et al. (2017) proposed a mechanism to stabilize CO_2 partial pressure in the atmospheres of water worlds by accounting for a wind-driven surface circulation and sea ice formation at higher latitudes (see also Ramirez & Levi 2018). To date, hydrosphere structures, CO_2 contents, and CO_2 reservoirs in the interiors of these CO_2-rich water worlds are poorly constrained, and this is what we aim to study here.

Here we build a planet interior structure model using the latest results from experimental data on the CO_2–H_2O system to explore the CO_2 budget and localize the main CO_2 reservoirs inside of water worlds. The classical models of water worlds (Kuchner 2003; Léger et al. 2004; Selsis et al. 2007) considered layered structures determined by the phase boundaries of pure water. As a first application of our new water world interior structure model, we perform the thought experiment of considering complete saturation in CO_2 of these water-dominated layers. By quantifying the maximum amount of CO_2 possibly stored inside each of these water-rich layers, we assess whether cometary amounts of CO_2 can be accommodated in the classical structure models for water worlds.

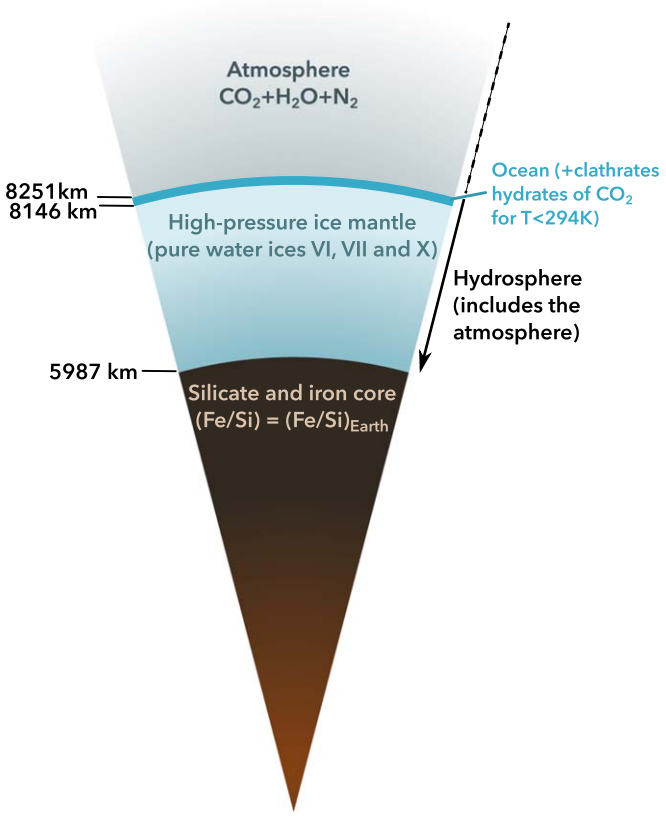

Figure 1. Example of the interior structure of a water world for 33% of water by mass and an isotherm of 300 K in the ocean. Layer thicknesses are true to scale.

Section 2 describes the thermodynamic and planetary model that we developed. We apply the model to quantify the potential saturated and excess CO_2 reservoirs in the hydrospheres of water worlds in Sections 3 and 4, respectively. We discuss the limitations of our model and uncertainties of the current equations of state (EOSs) in Section 5 and summarize our conclusions in Section 6.

2. Model

We consider H_2O- and CO_2-rich fully differentiated planets. The internal structure of these planets is differentiated into a rocky core with a roughly Earth-like Fe/silicate ratio surrounded by upper volatile-rich layers, which we call the "hydrosphere" (see Figure 1). Our study focuses on the structure of the hydrosphere.

Depending on the temperature and pressure profile in the hydrosphere, phases such as high-pressure ice, clathrate hydrates of CO_2, solid or liquid CO_2, liquid water, or gas could form (Figure 2). We compute the partitioning of water and CO_2 between these phases for a range of planetary masses (M_p), volatile (H_2O+CO_2) mass fractions respective to the total planet mass ($X_v = M_v/M_p$, where $M_v = M_{H_2O} + M_{CO_2}$ is the total volatile mass), the mass fraction of CO_2 relative to the

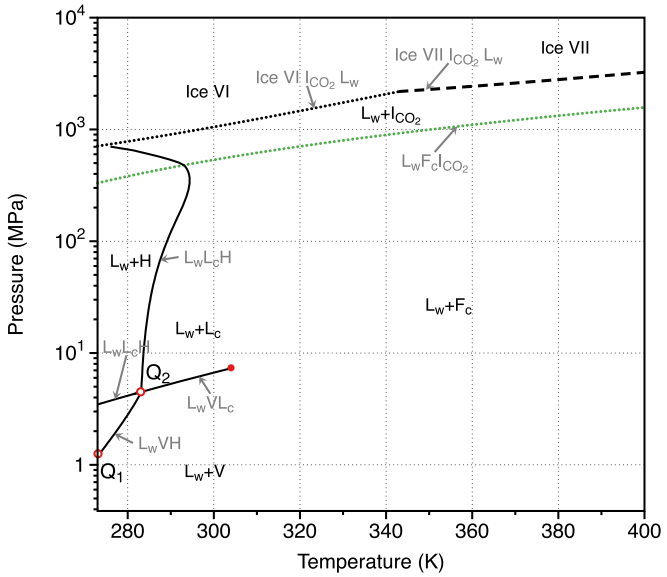

Figure 2. The P–T projection of the CO_2–H_2O phase diagram, showing the two- and three-phase coexistence curves and CO_2 critical point. Annotations specify the various phases, including the vapor phase V, water-rich liquid L_w, CO_2-rich liquid L_c, fluid CO_2 phase (above the critical temperature of CO_2) F_c, hydrate phase H, CO_2 ice I_{CO_2}, and ices VI and VII. The filled red circle denotes the critical point of CO_2, while the open red circles Q_1 and Q_2 are quadruple points where there is a coexistence of liquid water, vapor, hydrate, and water ice Ih (Q_1) and liquid water, vapor, hydrate, and liquid CO_2 (Q_2). The ice curves are from Abramson et al. (2017), the clathrate curve is from TREND (see the comparison with the experimental data Figure 3), and the values of the quadruple points and the triple lines that cross them are from Wendland et al. (1999).

total volatile mass ($X_{CO_2} = M_{CO_2}/M_v$), and an assumed temperature–pressure profile. As a result, we obtain an internal structure of the hydrosphere or the separation of the hydrosphere into several layers assuming thermodynamic equilibrium. For this study, the silicate and iron parts of the planet contribute to the model only in setting the mass–radius boundary conditions at the base of the hydrosphere.

As we explore planets with surface water oceans, the surface temperature (i.e., the temperature at the ocean–atmosphere interface) must be between 273.15 and 400 K. For surface temperatures lower than 273.15 K, the ocean has an icy crust at its surface, which would make the liquid water ocean challenging to detect by current and planned surveys. At the other extreme, ∼400 K is the highest temperature for life as we know it (Holden & Daniel 2010; Corkrey et al. 2014).

We focus on planets with sufficient water to form high-pressure ice mantles, wherein reactions between the silicate rocks and liquid water are suppressed and assumed to be negligible. This assumption is commonly made in the study of water worlds (e.g., Fu et al. 2010; Kitzmann et al. 2015; Levi et al. 2017). The absence of significant liquid water–rock chemical interactions has two important consequences for the internal structure and CO_2 reservoirs of water worlds. First, though formation of carbonates—the entrapment of CO_2 as (Ca, Mg, Fe)CO_3—is an important carbon reservoir on the Earth, it is negligible for water worlds. Second, in the absence of additional chemical agents that could drive the pH (i.e., salts) and increase the speciation of CO_2, we can use the EOS for pure H_2O–CO_2 mixtures to model water worlds. We further discuss and quantify the effect of water–rock interactions in Section 5.3.

Figure 2 shows the possible phases of CO_2+H_2O mixtures over the temperature and pressure ranges relevant to habitable water worlds. Areas between lines represent ranges of temperatures and pressures where one phase can exist or two phases are in equilibrium. Lines trace two- or three-phase equilibria. Lastly, points mark both specific combinations of temperature and pressure where four phases are in equilibrium (also called quadruple points) and the critical point of CO_2. Vapor (V) and water-rich liquid phases (L_w) coexist in equilibrium at the low-pressure end of this diagram. At higher pressures ($P \gtrsim 1.2$ MPa) and low temperatures ($T < 294$ K), CO_2+H_2O mixtures form a phase called clathrate hydrate. Clathrate hydrate is a crystalline structure consisting of a lattice of water molecules organized as cages entrapping guest molecules (in this case, CO_2). For the structure to be stable, guest molecules have to occupy a minimum fraction of the water cages. The total occupancy of the cages varies with temperature and pressure (Sloan & Koh 2007). Clathrate hydrates naturally occur on Earth (Sloan & Koh 2007), and their presence has been hypothesized on Mars (e.g., Kite et al. 2017) and icy satellites (Tobie et al. 2006; Choukroun et al. 2010).

For even higher pressures ($P \gtrsim 4.5$ MPa), CO_2 may condense in a liquid (noted as L_c in Figure 2). Under these conditions, instead of a vapor–liquid equilibrium, we have a liquid–liquid equilibrium with a water-rich liquid and a CO_2-rich liquid. For the highest range of pressures explored in this study (480 MPa and above), CO_2 ice (I) and polymorphs of high-pressure water ice form.

2.1. Atmosphere

We use the 1D radiative-transfer/climate model CLIMA, originally developed by Kasting & Ackerman (1986) and most recently updated in calculations of the HZs of Earth-like exoplanets (Kopparapu et al. 2013, 2014). CLIMA uses a correlated-k method to calculate the absorption coefficients of spectrally active gases both for the incoming shortwave stellar radiation (in 38 solar spectral intervals ranging from 0.2 to 4.5 μm) and for the outgoing longwave IR radiation (in 55 spectral intervals spanning wavenumbers from 0 to 15,000 cm^{-1}). The two-stream multiple scattering method of Toon et al. (1989) is used to calculate the radiative heating rate in each of the 101 atmospheric layers. For the inner edge of the HZ, the assumed atmospheric pressure–temperature profile consists of a moist pseudoadiabat extending from the surface up to an isothermal (200 K) stratosphere as described in Kasting (1988, Appendix A). For the outer edge of the HZ, a moist H_2O adiabat is assumed in the lower troposphere, and when condensation was encountered in the upper troposphere, a moist CO_2 adiabat is used, as described in Appendix B of Kasting (1991).

In this study, we focus on "habitable" water worlds, or water worlds with liquid water at their surfaces. In these cases, gases in the atmosphere are dissolved in the ocean. To place an upper limit on the volatile content of saturated reservoirs, we assume the atmosphere species are in thermodynamic phase equilibrium with the liquid water layer. Consequently, at the interface between the ocean and the atmosphere, the temperature, pressure, and chemical potentials of all of the chemical species constituting these layers are equal.

While CLIMA handles the calculation of the atmospheric radiative transfer and pressure–temperature profile in our model

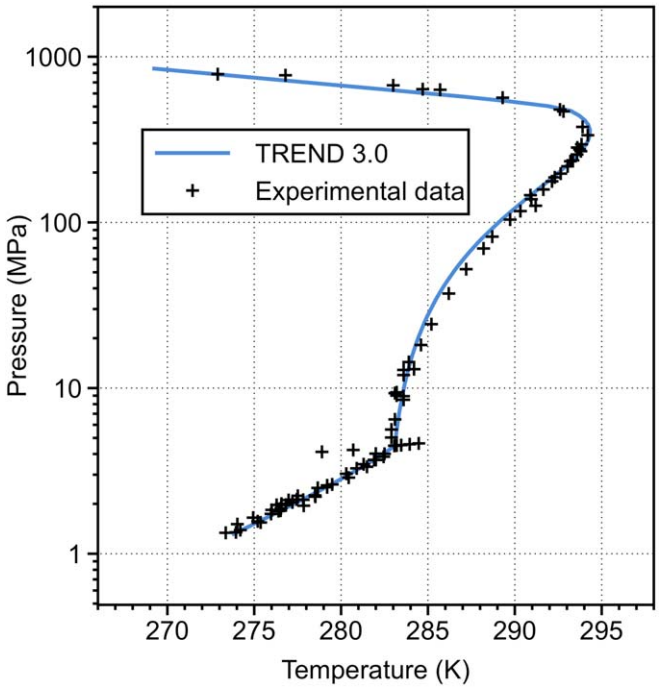

Figure 3. Comparison between the prediction of TREND 3.0 and the experimental data for the triple line CO_2 clathrates/liquid water-rich phase/CO_2-rich fluid phase. Experimental data are summarized in Sloan & Koh (2007).

of water worlds, phase changes and equilibria occurring in the fluid and solid water-rich layers of the hydrosphere are computed using TREND 3.0 software (Span et al. 2016).

2.2. EOS for CO_2–H_2O Mixtures

To estimate the potential CO_2 reservoirs of HZ water-rich exoplanets, we need to model the behavior of CO_2–H_2O mixtures at temperatures corresponding to "habitable" planet surfaces (273–400 K) and pressures up to the formation of high-pressure ice (~3.2 GPa). For this temperature range and at low-to-moderate pressures (up to a few MPa), there are numerous EOSs for the H_2O–CO_2 system that compute both the behavior of individual phases and phase equilibria (e.g., Carroll et al. 1991; Spycher et al. 2003; Hu et al. 2007). However, computing the behavior of CO_2+H_2O mixtures up to several GPa is currently still a challenge due to the lack of experimental data in the region of pressures above ~1 GPa. The recent study of Abramson et al. (2017) provides the first experimental data in this high-pressure region.

We use the state-of-the-art TREND 3.0 (Gernert & Span 2016) to model H_2O–CO_2 mixtures. TREND 3.0 is the reference EOS in the carbon capture, storage, and transport industry, and is (to our knowledge) the best option to reproduce the behavior of the CO_2–H_2O system in the temperature and pressure ranges of relevance to ocean-bearing water worlds (Gernert & Span 2016). TREND 3.0 reproduces all of the available experimental data of the CO_2–H_2O system for pressures up to 100 MPa with low errors (typically lower than 2%; see, e.g., Figure 3 or detailed comparisons in Gernert & Span 2016). TREND 3.0 is the result of decades of development by specialists in fluid behavior and construction of EOSs. We describe TREND 3.0 in detail below.

The model for CO_2–H_2O mixtures implemented in TREND 3.0 uses two empirical EOSs for pure fluids, explicit in Helmholtz free energy: one for water (IAPWS; Wagner & Pruß 2002) and one for CO_2 (Span & Wagner 1996). Provided density ρ and temperature T as independent variables, these EOSs compute the ideal and residual parts of the Helmholtz energy and their first, second, and third derivatives. By combining these derivatives, all thermodynamic properties can be calculated, including thermodynamic potentials u (specific internal energy), h (specific enthalpy), g (specific Gibbs free energy), p (pressure), s (specific entropy), and C_p (heat capacity at constant pressure), to cite few of them. See the complete list of thermodynamic properties in Table 6.3 of Wagner & Pruß (2002) and Table 3 of Span & Wagner (1996).

The range of temperature–pressure compositions where reliable experimental data exist defines the initial range of validity of the pure water and pure CO_2 EOSs. For pure water, IAPWS is valid up to 1273 K and 1 GPa, and for pure CO_2, the primary range of validity of the EOS goes up to 1100 K and 800 MPa. However, special care has been taken to ensure that these EOSs yield reasonable results when extrapolated beyond this initial range of validity. The density of water predicted by extrapolating IAPWS up to 3.5 GPa deviates from the experimental data of Wiryana et al. (1998) by no more than 3.5%. For CO_2, the EOS of Span & Wagner (1997) reasonably describes the behavior of the pure substance along the Hugoniot curve up to the limits of the chemical stability of carbon dioxide (see Figure 36 of Span & Wagner 1996). Moreover, both of these EOSs perform well when compared to ideal curves up to very high pressures and temperatures. Ideal curves (as defined by Span & Wagner 1997) are curves along which one property of a real fluid is equal to the corresponding property of the hypothetical ideal gas at the same temperature and density. Comparison to ideal curves has been shown to reliably predict the quality of extrapolations of empirical EOSs for pure substances (Deiters & De Reuck 1997; Span & Wagner 1997; Span 2013).

To combine the EOSs of pure compounds and compute the properties of various phases of CO_2–H_2O mixtures, TREND 3.0 blends multiple approaches that we detail in the following paragraphs. The overall methodology of TREND 3.0 is to compute the Gibbs energy of the CO_2–H_2O mixture at a given p and T and overall molar composition z and then minimize it. TREND 3.0 then determines which phases are stable at the provided T, p, and z; the density of all stable phases; and the molar composition of each of these phases. Once the above parameters are evaluated, TREND 3.0 computes the thermodynamic and calorific properties of each phase. For details of the algorithms used in TREND 3.0, refer to Kunz et al. (2007).

To compute the behavior of the CO_2–H_2O mixture from the pure fluid EOSs, TREND 3.0 uses mixing rules from Kunz et al. (2007) as adapted in Gernert & Span (2016). The mixing parameters are derived by fitting the experimental data of the CO_2–H_2O system, which includes the small amount of CO_2 dissociated in HCO_3^- and CO_3^{2-}. Consequently, the resulting EOS that is fitted to these data implicitly accounts for this dissociation, in the absence of other solutes.

TREND 3.0 is widely used in the carbon capture and storage (CCS) community and is regularly updated upon the arrival of new experimental data (e.g., Kunz et al. 2007; Kunz & Wagner 2012; Løvseth et al. 2018). The model described in

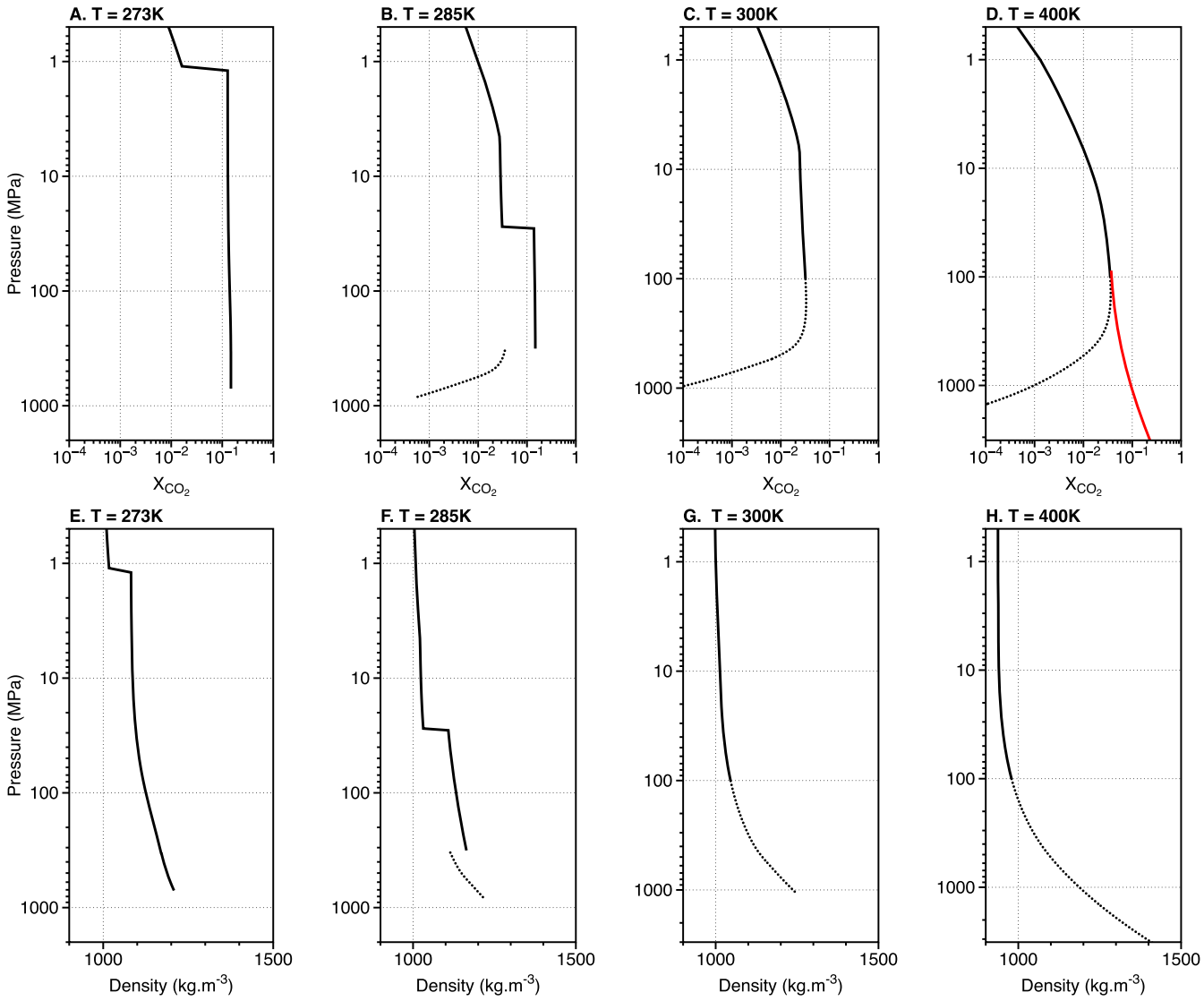

Figure 4. Molar fraction of CO_2 (panels (a)–(d)) and density (panels (e)–(h)) profiles of CO_2-saturated water worlds for isothermal ocean profiles at $T = 273$, 285, 300, and 400 K. Dotted lines denote pressures outside of the TREND 3.0 range of validity. The red line in panel (d) shows compositions interpolated from the experimental data of Abramson et al. (2017) for $T = 373$ K. Abrupt changes in composition and density denote phase transitions (see details in the text). Each profile is plotted until it reaches the pressure of formation of high-pressure water ice. Profiles inside the high-pressure ice phases are not shown.

Gernert & Span (2016), EOS-CG, is based on the mathematical structure introduced in the GERG-2004 and GERG-2008 approaches (Kunz et al. 2007; Kunz & Wagner 2012) but is explicitly developed to provide an accurate description of the CO_2–H_2O mixture. The initial range of validity of EOS-CG extends up to 500 K and 0.1 GPa; within these ranges, the carefully vetted experimental data sets on CO_2–H_2O mixtures to which EOS-CG is fit agree to within $\pm 2\%$ on the density of the mixture and ± 0.3 mol% on the solubility of CO_2 in water. Gernert & Span (2016) could not extend the EOS-CG model fit to higher pressures and temperatures due to significant disagreements in the density and/or solubility measurements between experimental data sets; no data set could be identified as significantly more accurate than the others. Tests have shown that this mixing rule can reasonably be used outside the extended range of validity if larger uncertainties are acceptable (Kunz & Wagner 2012). An estimate of the error introduced by extrapolating EOS-CG above >0.1 GPa is shown in Figure 4(d).

The EOS-CG model successfully describes the fluid phase that is in equilibrium with dry ice or CO_2 hydrate (Gernert & Span 2016). TREND 3.0 detects the formation of CO_2 ice I using the model detailed in Jäger & Span (2012), which proposes a thermal EOS for solid carbon dioxide that is explicit in Gibbs energy. The initial range of validity of this EOS is 80 K $< T <$ 300 K and 0 MPa $< T <$ 500 MPa. However, even when compared to experimental data with pressures up to 10 GPa (for a 296 K isotherm; Olinger 1982; Liu 1984), this EOS reproduces the density of solid CO_2 within 3%.

The formation of CO_2 clathrate hydrate is computed using the model described in a series of three papers: Jäger et al. (2016) and Vinš et al. (2016, 2017). The model is inspired by Sloan & Koh (2007) and based on the statistical van der Waals and Platteeuw approach (Van der Waals & Platteeuw 1959). It computes the chemical potential of water in the hydrate lattice, μ_w^H. Typically, if this chemical potential is lower than the chemical potential of liquid water computed with EOS-CG, then the clathrate hydrate phase is stable.

Vinš et al. (2016) showed that the lattice parameter of hydrates and the Langmuir constants that quantify the molecular interactions between the water lattice and CO_2 guest molecule strongly influence the computed value of μ_w^H. The water lattice parameter of clathrate hydrates is especially important at high pressures, while the Langmuir constant affects the computed filling fraction of the clathrate cages and therefore for the amount of CO_2 trapped in the clathrate layer. Vinš et al. (2017) described the fitting procedure to obtain all of the necessary model parameters. Jäger et al. (2016) provided the result of the fitting, assessed the performance of this model, and detailed its implementation in TREND 3.0. For the CO_2–H_2O mixture, this new model performs better when compared to previous formulations (e.g., Ballard & Sloan 2002a, 2002b). This model is valid for the whole range of temperature, pressure, and compositions of interest in this study (T = [273 K, 400 K], P up to ~700 MPa; see Figure 3).

TREND 3.0 does not account for the formation of high-pressure water ice. To detect the phase boundary of high-pressure water ice in contact with CO_2 ice, we use the scaling laws of Abramson (2017) for ices VI and VII. In that study, the authors obtained and fitted experimental data for the triple line CO_2 ice/high-pressure water ice (either VI or VII, depending on the temperature)/liquid water. This triple line shows considerable deviations from the pure water system (e.g., a difference of 0.22 GPa for $T = 363$ K). Thus, water-planet interior structure models that rely on the phase boundaries of pure water could incur significant errors.

For the EOS of ices VI, VII, and X (for the density and adiabatic temperature profiles of these phases), we use the formulation and parameters summarized in Noack et al. (2016).

2.3. Interior Structure of a Water World

We use a planet interior structure model to self-consistently compute the radii and hydrosphere structure of water worlds (Figure 1).

As inputs to the model, we specify the mass of the planet's rocky core $M_{\rm rock}$ (assumed to have an Earth-like silicate-to-iron mass ratio), the planet's volatile mass $M_v = M_p - M_{\rm rock} = X_v M_p$, and surface temperature. We assume an isothermal temperature profile in the liquid and clathrate layers and an adiabatic temperature profile in the high-pressure ice layers (Fu et al. 2010; Noack et al. 2016).

To model a planet, we guess an initial planet radius (defined at the ocean–atmosphere boundary). Then, we integrate the equations of hydrostatic equilibrium and the mass in a spherical shell inward through the hydrosphere toward the center of the planet (with care to use the EOS of the appropriate phase). We continue integrating inward until the total mass balance of volatiles is satisfied (i.e., when the integrated mass of the hydrosphere equals M_v). We then compare the radius at the water–silicate boundary obtained from the integration, $R_{\rm wsb}$, to the radius $R_{\rm rock}$ of an Earth-composition core of mass $M_{\rm rock}$ under the pressure overburden of the volatile envelope. Here $R_{\rm rock}$ is derived by interpolating the models for rocky cores from Rogers et al. (2011). If $R_{\rm wsb}$ and $R_{\rm rock}$ are too disparate, we adjust the radius of the planet at the ocean/atmosphere interface and repeat the inward integration through the hydrosphere. We iterate until $R_{\rm wsb}$ and $R_{\rm rock}$ correspond with an error less than 0.1%.

By modeling isothermal oceans saturated with CO_2, we set a strict upper limit on the CO_2 mass dissolved in water and trapped in clathrates. Adiabatic temperature profiles are associated with convection. Convection would lead to mixing and evolution toward a near-constant concentration of CO_2 through the ocean mediated by the CO_2 partial pressure in the atmosphere. Because the solubility of CO_2 increases with pressure (Section 3.1), the solubility of CO_2 in the liquid ocean is at its lowest at the ocean–atmosphere interface. Consequently, convecting adiabatic oceans would lead to lower CO_2 contents for the planet than those estimated with isothermal saturated ocean profiles. Further, an adiabatic temperature profile within the clathrate layer would lead to thinner clathrate layers because of the increase in temperature with depth. This would, in turn, diminish the clathrate layer's capacity as a CO_2 reservoir.

There is also physical motivation to consider nonconvecting oceans on water worlds. Levi et al. (2017) showed that oceans in water worlds might not possess a deep overturning circulation due to the lack of an energy source. The circulation in Earth's ocean relies on winds, lunar and solar tidal forcing, and the subsequent turbulent dissipation of internal waves on the seafloor topography. Water worlds do not have strong topography at the oceanic floor, and the depth of the ocean of these planets is considerably more important than that of the Earth's ocean, requiring significant energy sources for a steady-state global circulation. Levi et al. (2017) showed that winds on water worlds could provide enough energy for convection inside of an ~1 km surface layer. If the internal heat flux on these planets is low (Levi et al. 2014), then the temperature profile inside the ocean will be conductive.

3. CO_2 Content of Saturated Reservoirs

3.1. Description of Saturated Reservoirs of Water Worlds

The hydrospheres of water worlds present a variety of structures, depending on temperature. Examples of these possible ocean structures are plotted in Figure 4. In this figure, all of the profiles are plotted for an atmospheric pressure of 5 bars. We show in Section 4.1 that the amount of CO_2 in the atmosphere does not influence the results displayed in Figures 4 and 5.

For temperatures between 273 and 279 K, CO_2 solubility increases with pressure in the liquid ocean until 1.2 MPa, where a thick CO_2 clathrate hydrate layer forms. Figures 4(a) and (e) show an example of this profile for a $T = 273$ K ocean isotherm. The phase transition from liquid water to clathrate is marked by a sudden jump in the CO_2 molar fraction and density. This clathrate layer is immediately in contact with the high-pressure water ice at $P = 710$ MPa.

For ocean isotherms between 279 and 294 K, water-world hydrosphere structures display two oceans: one on top of the clathrate layer and another one under the clathrate layer, immediately in contact with the high-pressure ice. Figure 4 displays an example of this second type of hydrosphere structure for a 285 K ocean isotherm (panels (b) and (f)). Both density and composition profiles exhibit two phase transitions, one at 28 MPa and another at ~600 MPa. The second phase transition occurs when the clathrate layer becomes unstable at higher pressures. This is due to the inversion of the slope of the L_wL_cH triple line (liquid water/liquid CO_2/clathrate hydrates) for pressures higher than 350 MPa (see Figure 2).

Clathrate hydrates contain up to 15 mol% of CO_2, while the solubility of CO_2 in the global liquid ocean does not exceed

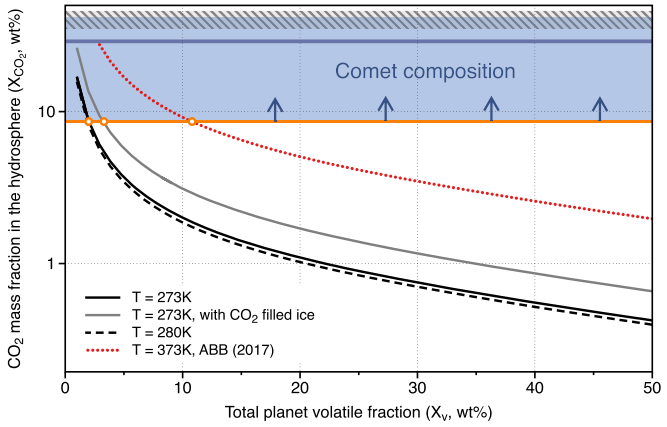

Figure 5. Hydrosphere saturated reservoir CO_2 storage capacity. The total mass fraction of CO_2 in the hydrosphere is plotted as a function of the bulk mass fraction of volatiles of the planet for several oceanic isotherms. The low X_v extreme of each curve is defined by the minimum volatile mass fraction at which the water worlds develop a high-pressure water ice mantle. The red line adopts CO_2 solubility interpolated from the experimental data of Abramson et al. (2017). The gray line includes, in addition to the CO_2 dissolved in the ocean and trapped in clathrates, the possible contribution of the CO_2-filled ice (see Section 3.3). The range of CO_2 fractions shaded in blue shows the range of mass fractions detected in comets (Mumma & Charnley 2011; Ootsubo et al. 2012), and the blue line shows the median value of this sample. The striped region shows the range of CO_2 fractions in low-mass protostellar envelopes (Öberg et al. 2011). The lowest mass fraction of CO_2 observed in comets is indicated by an orange line. On this figure, water worlds with X_v in excess of 1.9, 2.1, 3.5, and 11 wt% for isotherms of 280 and 273 K without and with CO_2-filled ice and 373 K, respectively, cannot accommodate comet-like amounts of volatiles in their saturated reservoirs.

~4 mol%, making clathrate hydrates the main CO_2 reservoir for ocean isotherms $T < 294$ K. The temperature of 294 K marks the stability limit of the clathrate phase; above it, clathrates are not stable at any pressure in the ocean. For $T = 300$ K (Figures 4(c) and (g)), the ocean is limited by the formation of high-pressure water ice. For the highest ocean temperature explored here, $T = 400$ K (Figures 4(d) and (h)), the liquid water region extends up to 3.2 GPa.

3.2. Mass Budgets of Saturated Reservoirs

We now evaluate the total CO_2 mass contained in the saturated reservoirs at a given temperature using the compositional profiles from Section 3.1. This mass is then divided by the total mass of the hydrosphere (M_v, including both CO_2 and water) to obtain the CO_2 fraction in the volatiles in the hydrosphere (X_{CO_2}; vertical axis of Figure 5). We vary the total amount of volatiles accreted by our model planets from $X_v = 1$ to 50 wt%. The main difference here between a planet that accreted 1 wt% volatiles and another that accreted 50 wt% is that the latter has a thicker high-pressure water ice mantle, considered here to be pure water ice. Consequently, the calculated CO_2 fraction in the volatiles of the planet's saturated reservoirs decreases as X_v increases. The cases that do not allow the formation of high-pressure water ice at the oceanic floor ($X_v \lesssim 3$ wt% at 373 and 400 K) are not displayed in Figure 5.

Figure 5 shows that, for cold oceans (i.e., sufficiently cold to form clathrates, <294 K), only planets that accreted a low ($X_v < 2$ wt%) bulk fraction of volatiles could store cometary abundances of CO_2 in their saturated reservoirs. In this temperature regime, decreasing temperatures lead to the formation of thicker CO_2 clathrate layers (because clathrates of CO_2 are stable over a larger pressure range). Since clathrates can store more CO_2 per unit mass than the liquid ocean (see Figure 4), the ability of the hydrosphere to store CO_2 in the saturated reservoirs increases as ocean temperature decreases. However, Figure 5 shows that water worlds with cold oceans reach comet-like compositions (above the orange line) for a very limited range of total planet volatile fractions ($X_v < 2$ wt%). Consequently, most of the water worlds possessing relatively cold hydrospheres would be unable to store comet-like amounts of CO_2, even if the ocean and the clathrate layers are both fully saturated.

For $T > 294$ K, the clathrate layer is not stable, and CO_2 dissolved in liquid water becomes the dominant saturated reservoir. This leads to low CO_2 fractions in the hydrosphere not exceeding 0.01 wt% for our highest-temperature isotherms (300 and 400 K).

3.3. Contribution of CO_2-filled Ice

Between pressures of ~0.6 and 1 GPa, the CO_2–H_2O system can form a phase called CO_2-filled ice (Hirai et al. 2010; Bollengier et al. 2013; Tulk et al. 2014; Massani et al. 2017). This corresponds to a compressed hydrate phase, where CO_2 molecules fill the channels formed by the molecules of water. Above 1 GPa, this phase dissociates to CO_2 ice and ice VI. The presence of CO_2-filled ice has been investigated from 80 up to 277 K. Amos et al. (2017) estimated the mass ratio between CO_2 and water molecules in this phase to be 41 wt%. Using this result, we estimate the size of the potential CO_2 reservoir in CO_2-filled ice and its influence on the hydrosphere CO_2 fraction, plotted as a gray line in Figure 5. We find that CO_2-filled ice can make a modest contribution to the total CO_2 budget of the water world. The presence of this phase adds between $\lesssim$1 and ~10 wt% to the total fraction of CO_2 in the hydrosphere, allowing habitable water worlds with X_v up to 3.5 wt% to reach comet-like CO_2 abundances (compared to the limit of $X_v < 2.1$ wt% in the absence of CO_2-filled ice). Consequently, the contribution of CO_2-filled ice does not significantly extend the range of the total planet volatile fractions of water worlds that could store comet-like fractions of CO_2 inside their saturated reservoirs.

3.4. Effect of CO_2 Dissociation at High Pressures and Temperatures

As warned by Gernert & Span (2016), the computation of the solubility of CO_2 in water by TREND 3.0 becomes more and more uncertain above ~100 MPa. Recent experiments on the CO_2–H_2O system of Wang et al. (2016) and Abramson et al. (2017, 2018) and the ab initio simulations of Pan & Galli (2016) show that CO_2 strongly dissociates and forms carbonic acid (H_2CO_3) at high pressures and temperatures ($P \gtrsim 1$ GPa, $T \gtrsim 373$ K). This leads to a much higher solubility of CO_2 at high pressures than predicted by TREND 3.0 (or that could be predicted by any of the currently available EOSs of the CO_2–H_2O system; see Abramson et al. 2017 for a detailed discussion).

In Figure 4(d), we plot in red the solubility of CO_2 in the liquid water ocean for $T = 373$ K provided by the interpolation of the experimental data of Abramson et al. (2017). The solubility of CO_2 at 400 K is expected to be very similar to that plotted for 373 K, because at pressures above 1 GPa, the isotherms display very similar compositions (see Figures 7 and 8 in Abramson et al. 2017). The solubility of CO_2 reaches

up to ~20 mol% at 3 GPa and 373 K (see the red line in Figure 4(d)).

The high-pressure dissociation of CO_2 investigated by Abramson et al. (2017) increases the CO_2 storage capacity of deep liquid oceans by more than 3 orders of magnitude in some cases (red line in Figure 5). For example, the CO_2 storage capacity goes from 0.01 wt% CO_2 at 400 K without the high-pressure dissociation to more than 10 wt% with it. This highlights the effect of uncertainties in the solubility of CO_2 at high pressures on the structure and maximal global saturated CO_2 reservoirs of water worlds. With the high-pressure dissociation of Abramson et al. (2017), the CO_2 storage capacity of the ocean at 373 K eclipses that of clathrates at temperatures below 294 K. We find that hot habitable water worlds may store cometary abundances of CO_2 in their water-dominated layers only if they initially accreted less than 11 wt% of volatiles by mass when the high-pressure dissociation of CO_2 is taken into account.

Even with the corrected solubility of CO_2 at high temperatures and pressures, water worlds' CO_2 storage is rather limited. The extent of the parameter space where water worlds are simultaneously habitable and able to accommodate comet-like CO_2 abundances in their saturated reservoirs is small, compared to all possible X_v and X_{CO_2}. In our study, the CO_2 fractions stored inside of the planets do not even reach the comet median abundances in CO_2. This result leads to a rather pessimistic outlook for the habitability of water worlds. If the excess CO_2 is not sequestered away in another reservoir during the water world's evolution (see Section 4.3), it will be degassed in the atmosphere and potentially induce surface temperatures that are too hot for life.

We expect that the impact of high-pressure dissociation on the CO_2 mass budgets calculated in Figure 5 will diminish with decreasing ocean temperature. Oceans at lower temperatures are shallower, reaching the interface between liquid water and high-pressure ice or clathrates at lower pressures. The CO_2 dissociation decreases with decreasing pressures, leading to lower CO_2 solubilities for pressures $\lesssim$1 GPa. Consequently, the red line in Figure 5 is an upper limit on the contribution of saturated reservoirs to the total CO_2 budget of water worlds.

4. CO_2 Content of Excess Reservoirs

For planets with high volatile mass fractions (more than 3.5 or 11 wt%, depending on the temperature), the liquid water ocean, clathrates, and CO_2-filled ice (if present) are insufficient to store comet-like amounts of CO_2. Here we propose possible excess reservoirs that CO_2 may form upon the saturation of the water-dominated phases: the atmosphere, liquid CO_2, CO_2 ice, and the monohydrate of carbonic acid ($H_2CO_3 \cdot H_2O$).

4.1. Atmospheres of Habitable Water Worlds

Using the CLIMA 1D radiative-convective model, we reproduce the boundaries of the water world HZ as a function of the partial pressure of CO_2 (first computed in Kitzmann et al. 2015; see our Figure 6). In these calculations, we assume a solar-mass star and an Earth-mass planet with an atmosphere containing 1 bar of N_2 and a range of CO_2 partial pressures. For visual reference, we have indicated the locations of the critical point and the quadruple points Q_1 and Q_2 of the CO_2–H_2O phase diagram (Figure 2). The limits of the HZ plotted here are uncertain due to the host star type, atmospheric

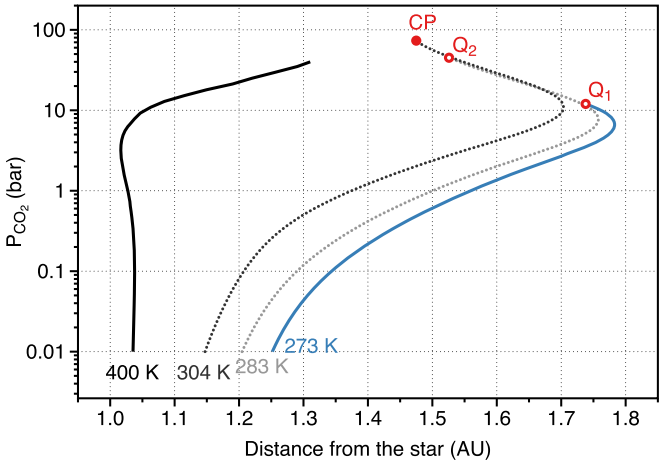

Figure 6. Distances from a Sun-twin host star where, for a given CO_2 partial pressure in the atmosphere, the planet surface keeps a constant temperature of either 400, 304, 283, or 273 K. A surface temperature of 400 K corresponds to the inner HZ limit adopted in this study (because it is the high-temperature limit for life as discussed in Section 2). The atmosphere is in the moist greenhouse state along the the 400 K line, so this inner limit is generous. The 273 K line corresponds to the CO_2-dependent outer edge of the HZ (see Section 2 and Kopparapu et al. 2013). For this figure, the partial pressure of N_2 has been fixed to 1 bar and the surface albedo of the planet to 0.06, corresponding to the albedo of the Earth's ocean. Here Q_1 and Q_2 are the quadruple points of CO_2 (same labels as in Figure 2), and CP shows the critical point of CO_2.

3D circulation, planet rotation rate, oceanic circulation, planet mass, and possibly other factors (e.g., Marshall et al. 2007; Yang et al. 2013; Kopparapu et al. 2014, 2017; Turbet et al. 2017; Kite & Ford 2018; Ramirez & Levi 2018). We use these 1D simulations only to estimate the possible atmospheric masses of CO_2 of habitable water worlds.

For a given distance from a Sun-like star, if the CO_2 content of the atmosphere exceeds the amount indicated by the black line, the surface temperature of this planet would exceed 400 K, and the water world would then be considered uninhabitable. We stopped our simulations for the inner edge of the HZ at a partial pressure of CO_2 of 40 bars because for higher pressures, the nonideal behavior of CO_2 must be taken into account, and CLIMA treats CO_2 as an ideal gas at temperatures above 303 K. For pure CO_2, the deviation from ideal pressure at 20 bars and ~400 K is of the order of 5%, while at 50 bars, it reaches ~20% (e.g., Duan et al. 1992; Hu et al. 2007). The addition of any other compounds (i.e., N_2 and H_2O) would only accentuate this error.

Figure 6 indicates that above a partial pressure of ~10 bars, the distance from the star to the inner edge of the HZ sharply increases (see also Kitzmann et al. 2015). An order-of-magnitude estimation—$M_{CO_2} = P_{CO_2} 4\pi R_p^2 / g$ for Earth values of M_p, R_p, and g—indicates that a CO_2 pressure of 100 bars represents a mass of the order of 5×10^{20} kg, corresponding to ~0.01 wt% of the total mass of the planet. Thus, CO_2 in the atmosphere would contribute at most $X_{CO_2} \lesssim 1$ wt% to the total volatile budget of the water world for the minimum $X_v \sim 1$ wt% that we consider, and even less for larger X_v. If the atmosphere of a water world holds more than a negligible fraction by weight of CO_2, the planet is not habitable.

We explored the influence of surface pressure on the CO_2 storage capacity of habitable water worlds. We reproduced the results of Figure 5 with an atmospheric pressure of 100 bars instead of 5 bars, finding no significant change ($\leqslant 10^{-3}$) in the final total CO_2 mass fractions of saturated reservoirs. Since we

are considering a fully saturated case, the profiles of X_{CO_2} with pressure throughout the ocean and clathrate layers (displayed in Figure 4) are unchanged; effectively, choosing a higher surface pressure of CO_2 only changes the low-pressure limit of the profiles. Since the atmosphere and ocean surface layer do not contribute significantly to the CO_2 storage capacity of habitable water worlds, our results are insensitive to the choice of CO_2 atmospheric partial pressure.

4.2. Condensation of Liquid CO_2

Liquid CO_2 is a potential excess reservoir for water worlds near the outer edge of the HZ with surface temperatures below the upper critical end point (UCEP) of the CO_2–H_2O system (304.5 K). At temperatures above the UCEP, liquid CO_2 will not condense at any pressure. Climate models of terrestrial planets have long recognized the possibility of condensation of CO_2 in Earth-like planet atmospheres and surfaces (Kasting 1991; von Paris et al. 2013). These studies focused, however, on the limits imposed by the saturation vapor pressure on the amount of CO_2 in planetary atmospheres, not on the liquid CO_2 condensate. The recent studies of Turbet et al. (2017) and Levi et al. (2017) investigated the possibility of condensation of liquid CO_2 and CO_2 clathrates at the poles of water-covered exoplanets.

For habitable water worlds, condensation of liquid CO_2 at the surface is possible only if the partial pressure of CO_2 in the atmosphere is at least $P_{CO_2} > 45$ bars and the planet temperature lies between the second quadruple point (283 K) and the UCEP (304.5 K) of the H_2O–CO_2 system. At temperatures below 283 K, CO_2 clathrates would form at the planet surface before liquid CO_2, assuming thermodynamic equilibrium. At temperatures above 304.5 K, CO_2 does not condense. Thus, surface liquid CO_2 oceans are stable in a rather narrow range of pressure and temperature conditions. Therefore, 3D simulations (e.g., Turbet et al. 2017; Ramirez & Levi 2018) are needed to assess the long-term stability of liquid CO_2 as a CO_2 reservoir at the surface of water worlds.

The density of liquid CO_2 varies considerably with temperature. Figure 7 shows that along its saturation line and for temperatures $T > 283$ K, the density of liquid CO_2 will be lower than the density of water, allowing it to float on top of the liquid water ocean. For temperatures $T < 273$ K, if CO_2 condenses before the formation of clathrates and in the presence of surface water ice, it will sink under the Ih ice layer, as described in Turbet et al. (2017). To determine the possible presence of large areas of liquid CO_2 on top of the liquid water ocean, one would need to account for temperature variations across the planet surface, heat redistribution, and CO_2 transport in the ocean and atmosphere. If a surface liquid CO_2 ocean is present, the atmospheric partial pressure of CO_2 would be at (or near) saturation.

At higher pressures (between 40 and 130 MPa, depending on temperature; Figure 7(b)), the density of fluid CO_2 can be higher than the density of liquid water. If CO_2 liquid–liquid phase separation occurs deep in the water ocean, i.e., at pressures higher than the line displayed in Figure 7(b), then the liquid CO_2 would be denser than the ambient water and sink toward the oceanic floor. There, the liquid CO_2 would cross the stability domain of CO_2 ice (see Figure 2), freeze, and sink into the high-pressure water ice mantle, as elaborated below (Section 4.3).

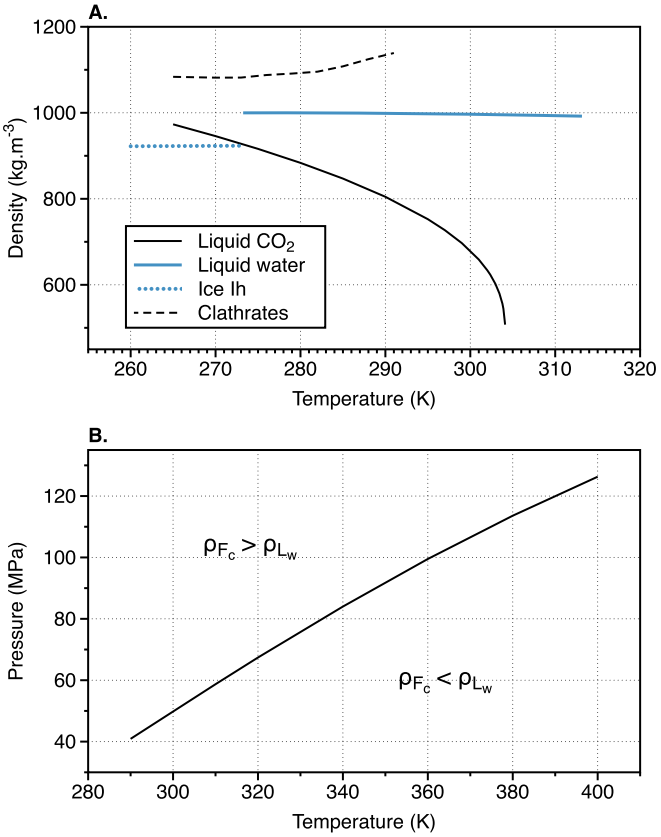

Figure 7. Comparison between densities of liquid water and liquid ($T < 304$ K) or fluid ($T > 304$ K) CO_2. Panel (a) compares the densities of liquid water, ice Ih, CO_2 clathrates, and liquid CO_2 at low/surface pressures ($P < 1$ bar at the saturation vapor pressures of each compound). The data plotted are from TREND 3.0 for liquid water, Choukroun & Grasset (2007) for Ih water ice, and Duschek et al. (1990) for liquid CO_2. Panel (b) shows pressure as a function of temperature on the dividing line where the density of the water-rich liquid and the CO_2-rich fluid are equal (from TREND 3.0).

4.3. CO_2 Ice as a Main Reservoir of CO_2 for Habitable Water Worlds

Water worlds may encounter the conditions for CO_2 ice formation within their hydrospheres as the planets evolve and cool. Whether the CO_2 ice forms before, during, or after the water world's high-pressure water ice mantle freezes determines the initial formation location of the CO_2 ice layer (be it under, within, or on top of the high-pressure water ice mantle; see also Section 5). Because the density of CO_2 ice is always higher than the density of high-pressure water ices VI and VII (Figure 8), CO_2 ice is stably stratified when buried under those layers. If the CO_2 ice is instead deposited on top of the high-pressure water ice later in the evolution of the planet, an unstable density stratification results, which could lead to gravitational Rayleigh–Taylor instabilities (and the eventual burial of CO_2 ice in the high-pressure water ice mantle).

We estimate the timescales for the development of a Rayleigh–Taylor instability in CO_2 ice deposited at the surface of the high-pressure ice mantle. The timescale for the development of a Rayleigh–Taylor instability (τ_{RT}) is the nominal time required to produce unit strain under a deviatoric stress of magnitude

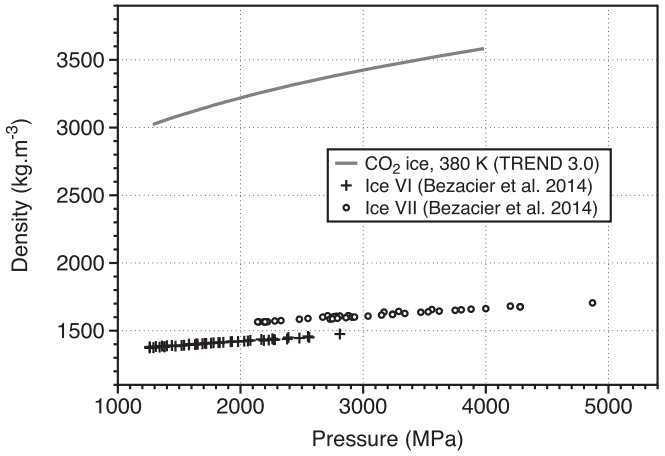

Figure 8. Comparison between the density of CO_2 ice and high-pressure water ices. We use TREND 3.0 to obtain the density of CO_2 ice as a function of pressure for a 380 K isotherm. Points are the experimental data of Bezacier et al. (2014) for ices VI and VII for temperatures ranging from 300 to 340 K and 300 to 380 K, respectively.

$g \times \Delta\rho \times H$ (e.g., Turcotte & Schubert 2014),

$$\tau_{\rm RT} = \frac{13.04\eta}{g\Delta\rho H}, \quad (1)$$

where η is the viscosity of the most viscous layer, g is the local gravitational acceleration, $\Delta\rho$ is the difference in density between the two layers, and H is the length scale, set here to the thickness of the CO_2 layer.

The most viscous layer controls the development of a Rayleigh–Taylor instability. For temperatures below 343 K, CO_2 ice is in contact with ice VI. Laboratory measurements of the viscosity of ice VI at high differential stresses ($\gtrsim 10^6$ Pa) give viscosities of the order of 10^{13}–10^{14} Pa s (Poirier et al. 1981; Sotin et al. 1985; Durham et al. 1996). The viscosity of CO_2 ice (I) for similar differential stresses is of the order of 10^{12}–10^{13} Pa s (Durham et al. 1999).

The extrapolation of the behavior of each material to planetary shear stresses must be handled with care. The creep behavior at the low shear stresses ($\lesssim 10^5$ Pa) relevant to planet interiors might be controlled by different mechanisms than those probed in experimental studies (Durham & Stern 2001). However, no experimental work to date has confirmed a change in creep behavior for ice VI and CO_2 ice at decreasing shear stresses. Therefore, to estimate the viscosity of ice VI and CO_2 in planetary conditions, we adopt the shear stress dependence provided in Poirier et al. (1981) and Durham et al. (1999), respectively. We obtain upper estimates of 10^{18} Pa s for ice VI and 10^{15} Pa s for CO_2 ice (Durham et al. 2010). Consequently, ice VI would control the formation of a Rayleigh–Taylor instability.

For temperatures above 343 K, CO_2 ice would be in contact with ice VII (Figure 2). To our knowledge, no experimental measurements of the viscosity of ice VII currently exist. The only theoretical study of the ice VII viscosity is found in Poirier (1982), where the author examined the crystalline lattice of ice VII and concluded that ice VII should have a high viscosity because its crystalline structure does not favor the propagation of dislocations. Thus, ice VII is likely more viscous than the CO_2 ice and would control the formation of a Rayleigh–Taylor instability at $T > 343$ K.

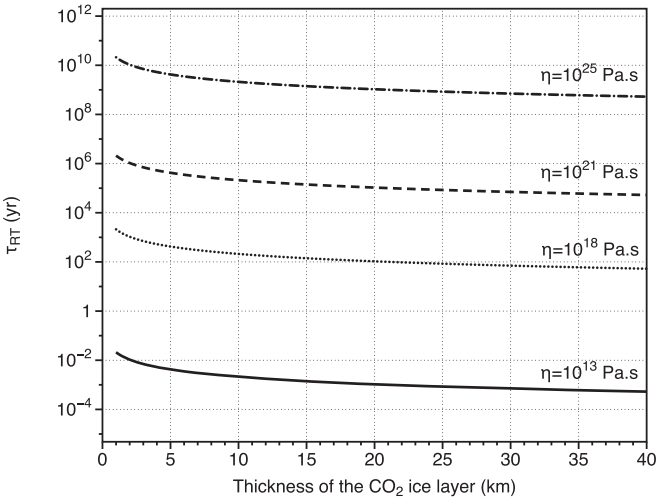

Figure 9. Timescales for the development of a Rayleigh–Taylor instability for a layer of CO_2 ice on top of the pure ices VI or VII. Due to the uncertainty of the viscosity of ices VI and VII for the planetary conditions, this figure displays a wide range of viscosities: $\eta = 10^{13}$ Pa s is the highest order-of-magnitude viscosity of ice VI experimentally measured by Poirier et al. (1981) and Durham et al. (1996); $\eta = 10^{18}$ Pa s is the extrapolation of these experimental measurements up to the planetary scales of Durham et al. (2010). For a visual reference, we also show the same timescales for $\eta = 10^{21}$ Pa s, the viscosity of the Earth's mantle, and for $\eta = 10^{25}$ Pa s, for which timescales of the development of the Rayleigh–Taylor instability start to be comparable to planetary ages.

Figure 9 shows timescales of the development of a Rayleigh–Taylor instability for several choices of η. The viscosity values span from the lowest viscosities experimentally measured for ice VI to $\eta = 10^{25}$ Pa.s, where the timescales to form Rayleigh–Taylor instabilities start to be comparable to the planetary ages.

For ice VI, the timescale of the development of a Rayleigh–Taylor instability is always short, less than 10,000 yr. Unless the ice VII viscosity is greater than $\eta = 10^{25}$ Pa s, CO_2 ice would also sink into the mantle in short timescales for temperatures higher than 343 K. We thus conclude that the formation of a CO_2 ice layer at any time during the thermal evolution of a water world would lead to its burial inside the high-pressure ice mantle.

If CO_2 is buried as CO_2 ice inside the high-pressure water ice mantle, the atmospheric CO_2 content would be decoupled from the total CO_2 content of the water world. Consequently, future observations of habitable water worlds' atmospheres would not provide the total CO_2 content of the planet but rather the CO_2 content of the atmosphere only. With models like the one presented in this study, it would be possible to estimate the amount of CO_2 dissolved in the global water ocean and trapped in clathrates for an assumed interior temperature profile. However, the masses of CO_2 ice that might be trapped in the high-pressure water mantle are independent of these measurements and would be more challenging to constrain with future observations.

4.4. Monohydrate of Carbonic Acid

The H_2O–CO_2 phase diagram is poorly characterized at pressures above ~1 GPa. A recent discovery is the formation of a carbon-bearing solid at high temperatures and pressures: the monohydrate of carbonic acid ($H_2CO_3 \cdot H_2O$; Abramson et al. 2017, 2018).

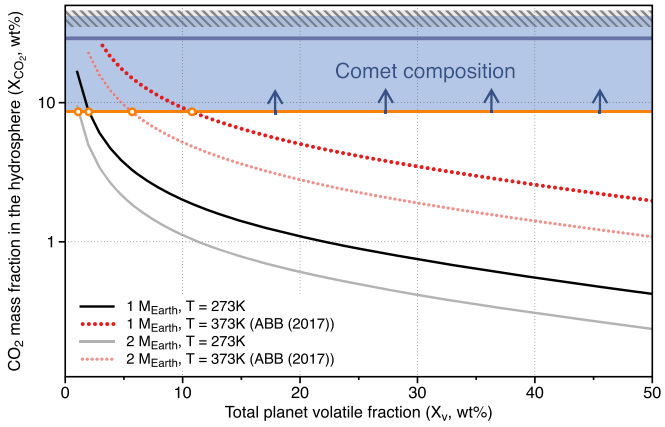

Figure 10. Dependence of hydrosphere saturated reservoir CO_2 storage capacity with M_{rock}. The total mass fraction of CO_2 in the hydrosphere is plotted as a function of the bulk mass fraction of volatiles of the planet for oceanic isotherms of 273 and 373 K. The $M_{rock} = 1\ M_{Earth}$ isotherms are the replication of the results displayed in Figure 5. Here ABB (2017) references the solubility obtained from the interpolation of the experimental data of Abramson et al. (2017). See the caption of Figure 5 for the description of the shaded/striped regions in the figure and the orange line.

Abramson et al. (2017) identified the presence of a stable solid phase in the H_2O–CO_2 system for $P > 4.4$ GPa. Abramson et al. (2018) then determined that this phase consists of a monohydrate of carbonic acid, measured its crystalline structure, and derived its density at $P = 6.5$ GPa and $T = 413.15$ K.

The temperatures and pressures at which the monohydrate of carbonic acid has been observed correspond to the conditions in the high-pressure ice layers of habitable water worlds. The density of this solid is higher than the density of ices VI and VII (2194 kg m^{-3}; Abramson et al. 2018; compare to Figure 8). Consequently, the monohydrate of carbonic acid will remain buried in the high-pressure ice layers and coexist with CO_2 ice. Both of these solids would constitute an excess reservoir of CO_2 that would sequester the carbon dioxide away from the atmosphere.

The stability field of the monohydrate of carbonic acid has not yet been mapped. It is still unclear if the monohydrate of carbonic acid (or other solids) forms at lower pressures and temperatures ($P < 4.4$ GPa and $T < 438.15$ K; see Saleh & Oganov 2016). Any future detection of solid compounds in the H_2O–CO_2 system at these conditions would impact the interior models of water worlds and icy satellites.

5. Discussion

5.1. Planet Mass Dependence

Our constraints on the CO_2 content of saturated reservoirs are more severe for planets with more massive rocky (iron and silicate) cores. For water worlds with $M_{rock} = 2\ M_{Earth}$ (with Earth-like Fe/Si values), cometary compositions would be compatible with habitable surfaces if the planets initially have less than 6 wt% of volatiles by mass (see Figure 10), compared to the limit of 11 wt% volatiles for planets with $M_{rock} = 1\ M_{Earth}$. More massive planets reach higher pressures in their hydrospheres due to their higher surface gravity. Consequently, they reach the stability field of high-pressure ice at lower depths. The ocean and the clathrate layers are thinner and store less CO_2 when compared to lower-mass planets with the same ocean temperature.

5.2. Metal Core as Another Potential Reservoir of CO_2

In this work, we have focused on CO_2 reservoirs within the hydrospheres (water-rich outer layers) of water worlds. Depending on the formation history of the planet, the rocky interiors of water worlds offer another potential CO_2 reservoir.

Experimental studies show that CO_2 and, more generally, carbon behave as siderophile elements and are more likely to dissolve in liquid iron than in silicate melts (e.g., Dasgupta et al. 2013). Carbon solubility in iron-rich liquids increases with pressure and decreases with increasing temperature, extent of hydration, and oxygen fugacity (Dasgupta et al. 2012, 2013). Previous studies have shown that from 5% to 10% of Earth's core is constituted of light elements (Birch 1964), with C as a plausible candidate along with H, S, O, and Si (Poirier 1994). Indeed, the iron core could be Earth's dominant carbon reservoir (Bergin et al. 2015; Hirschmann 2016). The exact composition in light elements of Earth's core is currently unknown, and the conditions for the C supply and the Earth's core formation continue to be subject to debate (see the summary in Dasgupta 2013). Likewise, the efficiency of CO_2 entrapment in the iron-rich liquid, in the context of the formation of differentiation of water worlds, is currently unexplored.

5.3. Entrapment of CO_2 as $CaCO_3$

On Earth, carbonates—(Ca, Mg, Fe)CO_3—are an important reservoir of CO_2. On Earth, carbonate minerals form when dissolved cations (such as Ca, Mg, and Fe) produced by silicate weathering react with carbonate ions, CO_3^{2-}, in the ocean. In this work, since we focus on planets with sufficient water to form high-pressure ice mantles, we have so far neglected reactions between the silicate rocks and liquid water (following, e.g., Léger et al. 2004; Selsis et al. 2007; Fu et al. 2010; Kitzmann et al. 2015; Levi et al. 2017) and thus also carbonate minerals as a CO_2 reservoir on water worlds. The formation of carbonates is impeded on a water world because (1) the high-pressure ice mantle creates a physical barrier between the ocean and silicates, (2) high pressures ($\gtrsim$0.6 GPa) at the silicate surface lead to a stagnant lid tectonic regime with little renewal of fresh silicates for weathering (Kite et al. 2009), and (3) incorporation of salts into high-pressure water ice can efficiently remove salts from the liquid ocean (Levi & Sasselov 2018). In this section, we elaborate further on the justification for this baseline assumption and set an upper limit on the capacity of carbonates as a CO_2 storage reservoir on water worlds.

The thick high-pressure ice mantles of water worlds may impede chemical exchanges between silicates and the liquid ocean on water-world planets. On water worlds, liquid water oceans may be separated from silicate rock by high-pressure ice mantles that are up to ~4000 km thick. In the case of Ganymede, Kalousová et al. (2018) showed that the melting of water at the base of the high-pressure water ice mantle and the transport of this water by convection to the upper liquid water ocean are favored only for thin ice mantles (<200 km) and high viscosities in the high-pressure ices. Kalousová et al. (2018) found that the transport of molten water from the base of the high-pressure water mantle to the liquid water ocean shut down for a mantle thickness greater than 400 km. While such detailed studies have not yet been accomplished for water worlds, this indicates a trend of weaker convection and

therefore fewer chemical exchanges for thicker high-pressure ice mantles.

On Earth, plate tectonics and volcanism continuously provide fresh silicates at the Earth's surface that replenish the source of cations for the carbonate formation. Kite et al. (2009) showed that, on water worlds, once the postaccretional magma ocean has solidified, high pressures ($\gtrsim$0.6 GPa) at the water–silicate interface curtail the volcanism. The resulting tectonic regime for the planet is a stagnant lid. Water worlds thus have a limited reservoir of silicates that would be available to supply cations to the ocean.

If salts are initially present in the water-world ocean, they will be removed on timescales of tens of millions to hundreds of millions of yr. Levi & Sasselov (2018) described a mechanism that can pump salts out of water-world oceans, sequestering them inside the high-pressure ice.

Despite the arguments above, it is still to be determined if the presence of a thick high-pressure water ice layer would fully impede chemical exchanges between the liquid water ocean and silicates. Water–rock interactions could occur during the early stages of planet formation (before the high-pressure ice mantle forms). They may also potentially occur during the later stages of the planet's evolution, if the heat flux at the top of the silicate layer allows for the melting of high-pressure ices (Noack et al. 2016; Kalousová et al. 2018).

We set an upper limit on the CO_2 storage capacity of carbonates in ocean-bearing water worlds, following a similar approach to that of Kite & Ford (2018). Kite & Ford (2018) estimated that in the most optimistic case (assuming the liquid water reacts efficiently with the silicates), liquid water would react with a layer of silicates at most ~50 km thick. These reactions would primarily form $CaCO_3$, as Mg and Fe cations are more to likely form silicates (see Kite & Ford 2018 for a detailed discussion). For the purpose of this calculation, we assume that the silicates are basalts (which are ubiquitous in the solar system). Basalts contain 11.39 wt% of CaO, so if all of the calcium reacts with CO_2 to form $CaCO_3$, it results in an entrapment of $\sim 7 \times 10^{21}\,(R_{\rm rock}/R_\oplus)^2$ kg of CO_2. This mass of CO_2 stored in the carbonates, when scaled to the total volatile mass of the planet, M_v, corresponds to

$$X_{CO_2} = 11\ \text{wt\%}\left(\frac{R_{\rm rock}}{R_\oplus}\right)^2\left(\frac{X_v^{-1}-1}{0.01^{-1}-1}\right)\left(\frac{M_\oplus}{M_{\rm rock}}\right). \quad (2)$$

For a water world with $M_{\rm rock} = 1\,M_\oplus$ and $R_{\rm rock} = 1\,R_\oplus$, carbonates can store an additional $X_{CO_2} = 11$ wt% when $X_v = 1$ wt% and only $X_{CO_2} = 2$ wt% when $X_v = 5$ wt%. Thus, carbonates may extend the storage capacity of CO_2 for water worlds with total volatile contents <5 wt% but represent a negligible CO_2 reservoir for planets with more massive volatile envelopes. Consequently, while carbonates could increase the CO_2 storage capacity in the hydrosphere at the low $X_v < 5$ wt% (leftmost) edge of Figures 5 and 10, the effect of carbonates is negligible over the rest of these figures. Our main conclusions still hold: water worlds with hydrospheres accounting for more than 11 wt% of the total planet mass require additional CO_2 reservoirs (beyond the liquid ocean, clathrates if present, atmosphere, and carbonates) to both accommodate cometary abundances of CO_2 and host a surface liquid water ocean.

5.4. Implications for Water World Habitability

Our models indicate that, in a majority of cases, water worlds with comet-like compositions will be too CO_2-rich to host a liquid water ocean on their surfaces. Indeed, for water worlds with more than 11 wt% of volatiles, the saturated (water-dominated) layers of the hydrosphere cannot store comet-like amounts of CO_2. Moreover, the 11 wt% limit is already generous. Our habitable water-world models almost never reach the median comet composition $X_{CO_2} \sim 29$ wt%. Our initial assumptions of an isothermal oceanic temperature profile and full saturation of CO_2 maximize the amount of CO_2 stored in the water-dominated saturated reservoirs. If water worlds are to be habitable, the excess CO_2 (i.e., the CO_2 that could not be incorporated in the saturated reservoirs) must be stored away from the ocean and atmosphere.

Whether, how many, and where liquid and/or solid CO_2 layers form depend on the evolution and accretion history and the global CO_2 fraction of the planet. To determine whether the excess CO_2 is more likely to degas in the atmosphere, form a liquid layer on top of the water ocean, or form CO_2 ice or a monohydrate of carbonic acid, one would need to model the postaccretional cooling of a water world's steam envelope from its initial hot state and determine at which pressures the CO_2–H_2O mixture saturates in CO_2. If this saturation is reached at low pressures (i.e., below the line of Figure 7(b)), condensed CO_2 is likely to float on the surface of a water ocean and/or evaporate in the atmosphere. Consequently, a potential outcome for the evolution of water worlds could be a hot hydrosphere consisting of an extended steam envelope that transitions from vapor to supercritical fluid to plasma at greater and greater depths (as has been considered by, e.g., Kuchner 2003; Rogers & Seager 2010; Nettelmann et al. 2011; Lopez et al. 2012). At high pressures, where CO_2 fluid is denser than water, the excess CO_2 would condense, sink, and precipitate as ice or a monohydrate of carbonic acid. Our results therefore indicate that further modeling of water-world cooling and formation will be crucial for determining how much CO_2 each of these excess reservoirs could store and whether cometary composition water worlds are likely to be habitable.

Previous studies (e.g., Kitzmann et al. 2015; Levi et al. 2017; Turbet et al. 2017; Ramirez & Levi 2018) have implicitly assumed that water worlds will form liquid water oceans if they are at an appropriate distance from the star and then derive an amenable CO_2 flux from the interior or CO_2 partial pressure in the atmosphere. Our work shows that the condensation of the high-pressure water ice layer, as well as a liquid water ocean, is not a given. Detailed 3D GCM modeling of water worlds with liquid water oceans is inapplicable if water worlds generically never manage to cool sufficiently to form liquid water oceans in the first place. Indeed, there is a tension between the likely comet-like compositions of volatiles accreted by water worlds and the amount of CO_2 that can be accommodated in the water-world structures modeled in previous works. It is possible that the sequestration of solid CO_2 in the high-pressure ice mantle, as we have proposed in Section 4.3, could save the habitability of water-world exoplanets, but detailed models of the postaccretional cooling of water worlds are needed to demonstrate this.

5.5. Effect of EOS Uncertainties

TREND 3.0 (and other cubic EOSs, when coupled to an appropriate clathrate model; i.e., Soave 1972; Gasem et al. 2001; Sloan & Koh 2007) can accurately set an upper limit on the mass of CO_2 that could be stored in the water-dominated layers of ocean-bearing water worlds at the outer edge of the HZ. For isotherms $T < 283$ K, the depth of the ocean is limited by the formation of clathrates to isostatic pressures not exceeding 100 MPa. Experimental data are widely available for pressure-dependent CO_2 solubilities in these relatively shallow surface oceans.

For ocean temperatures $T > 294$ K, water worlds have deep oceans and do not form clathrates. Current thermodynamic models (including cubic EOSs and TREND 3.0; for a review, see Abramson et al. 2017) strongly underestimate the amount of CO_2 dissolved in the deep liquid water ocean. This is likely due to the dissociation of CO_2 at high temperatures and pressures that has been investigated only recently (i.e., Pan & Galli 2016; Abramson et al. 2017) and is not included in the current EOSs for the CO_2–H_2O system. Accounting for the dissociation of CO_2 at high pressure and temperature greatly influences the total CO_2 budget of saturated reservoirs. In Figure 5, accounting for this effect adds more than 3 orders of magnitude in the total CO_2 storage capacity. Models that correctly reproduce the high solubility of CO_2 at the high pressure and temperature demonstrated by the recent experimental data are needed to assess the habitability of water worlds.

Moreover, the phase boundaries of a monohydrate of carbonic acid are currently poorly constrained (Wang et al. 2016; Abramson et al. 2018). The experimental work of Wang et al. (2016) shows that this solid could form at high pressures (>3.5 GPa) and high temperatures (1773 K), where neither high-pressure ice nor CO_2 ice yet condense. Therefore, the accumulation of the monohydrate of carbonic acid could start at the early stages of water-world postaccretional evolution, removing CO_2 from a supercritical envelope. Detailed models of the cooling of water worlds and the formation of such a reservoir are needed to understand if the removal of CO_2 by the precipitation of the monohydrate of carbonic acid would be sufficient to lead to an efficient cooling of water worlds and a subsequent condensation of liquid water and high-pressure phases of water ice. These models would necessitate further constraints on the location of the monohydrate of carbonic acid phase limit in pressure–temperature–composition space.

We hope that this paper will motivate new experimental and computational studies to further explore the phase diagram of the CO_2–H_2O system, specifically the dissociation of CO_2 in water at pressures above 1 GPa and the phase limit of the newly discovered solid monohydrate of carbonic acid.

6. Conclusions

We model the hydrosphere structures of water worlds. We use TREND 3.0, a state-of-the-art EOS widely used by the CCS community, to determine the maximum amount of CO_2 dissolved in water and trapped in clathrate hydrates as a function of temperature and pressure. We assume an isothermal profile in the liquid water and clathrates and an adiabatic profile in the high-pressure water ice mantle.

We determine that in the absence of an efficient CO_2 sequestration mechanism for CO_2, a water world that accreted more than 11 wt% volatiles during its formation cannot be habitable. The atmosphere, ocean, and clathrate layer of habitable water worlds with >11 wt% of volatiles by mass cannot accommodate comet-like, CO_2-rich compositions.

Water worlds that accreted a smaller mass fraction of volatiles could potentially store comet-like amounts of CO_2 in their saturated reservoirs, depending on their temperature profile. Even then, in our models, the saturated hydrospheres of habitable water worlds almost never reach the median comet composition of $X_{CO_2} \sim 29$ wt%.

If the excess CO_2 is not sequestered away from the atmosphere, HZ water worlds may be unable to cool sufficiently from their postaccretional hot state to condense liquid water oceans. The current paradigm of HZ water worlds as condensed super-Ganymedes should be expanded. Depending on their postaccretional cooling history, we may be more likely to observe HZ water worlds in hot uncondensed states with supercritical steam envelopes.

We stress that extrapolations of current EOSs to high pressures and temperatures ($P > 100$ MPa, $T > 400$ K) are unable to correctly predict the solubility of CO_2 in water. This is due to the dissociation of CO_2 at high pressures and temperatures and is an ongoing research frontier in material science. Our work demonstrates that the dissociation of CO_2 has crucial implications for the habitability of water worlds at the inner edge of the HZ.

Unless the C entrapment in the iron core was efficient during the accretion of water worlds, the largest potential reservoir of CO_2 in the hydrospheres of habitable water worlds is likely to be CO_2 ice and monohydrate of carbonic acid, trapped in the high-pressure water ice mantle. Consequently, the atmospheric composition of an ocean-bearing water world does not necessarily reflect the total mass of volatiles accreted during the formation of the planet or the relative proportions of CO_2 and H_2O in the hydrosphere.

More detailed modeling of the postaccretional cooling of water worlds is needed to determine whether CO_2 ice burial could allow water worlds to have liquid water oceans or whether the evolution of the planet would generically lead to too much atmospheric CO_2 for the planets to be habitable.

We thank the reviewers who provided helpful comments that served to improve this manuscript; R. Span for providing us with the TREND 3.0 software; S. Domagal-Goldman, R. Ramirez, and R. Kopporapu for their help and for providing us with ATMOS; and E. Kite for insightful discussions about water worlds. This work is supported by the NASA Habitable Worlds Program, grant No. 80NSSC19K0314.

ORCID iDs

Nadejda Marounina https://orcid.org/0000-0002-1197-6143
Leslie A. Rogers https://orcid.org/0000-0003-0638-3455

References

Abramson, E. H. 2017, JPhCS, 950, 042019
Abramson, E. H., Bollengier, O., & Brown, J. M. 2017, AmJS, 317, 967
Abramson, E. H., Bollengier, O., Brown, J. M., et al. 2018, AmMin, 103, 1468
Alibert, Y., & Benz, W. 2017, A&A, 598, L5
Amos, D. M., Donnelly, M.-E., Teeratchanan, P., et al. 2017, J. Phys. Chem. Lett., 8, 4295
Ballard, A. L., & Sloan, E. D. 2002a, Fluid Ph. Equilibria, 194, 371
Ballard, A. L., & Sloan, E. D., Jr. 2002b, J. Supramol. Chem., 2, 385
Beichman, C., Benneke, B., Knutson, H., et al. 2014, PASP, 126, 1134

Bergin, E. A., Blake, G. A., Ciesla, F., Hirschmann, M. M., & Li, J. 2015, PNAS, 112, 8965
Bezacier, L., Journaux, B., Perrillat, J.-P., et al. 2014, JChPh, 141, 104505
Birch, F. 1964, JGR, 69, 4377
Bockelee-Morvan, D., Crovisier, J., Mumma, M. J., & Weaver, H. A. 2004, in Comets II, ed. M. C. Festou et al. (Tucson, AZ: Univ. Arizona Press), 391
Bollengier, O., Choukroun, M., Grasset, O., et al. 2013, GeCoA, 119, 322
Carroll, J. J., Slupsky, J. D., & Mather, A. E. 1991, JPCRD, 20, 1201
Choukroun, M., & Grasset, O. 2007, JChPh, 127, 124506
Choukroun, M., Grasset, O., Tobie, G., & Sotin, C. 2010, Icar, 205, 581
Corkrey, R., McMeekin, T. A., Bowman, J. P., et al. 2014, PLoSO, 9, e96100
Dasgupta, R. 2013, RvMG, 75, 183
Dasgupta, R., Chi, H., Shimizu, N., Buono, A., & Walker, D. 2012, LPSC, 1659, 1767
Dasgupta, R., Chi, H., Shimizu, N., Buono, A. S., & Walker, D. 2013, GeCoA, 102, 191
Deiters, U. K., & De Reuck, K. M. 1997, PApCh, 69, 1237
Ding, F., & Pierrehumbert, R. T. 2016, ApJ, 822, 24
Duan, Z., Møller, N., & Weare, J. H. 1992, GeCoA, 56, 2605
Durham, W., & Stern, L. 2001, AREPS, 29, 295
Durham, W. B., Kirby, S. H., & Stern, L. A. 1999, GeoRL, 26, 3493
Durham, W. B., Prieto-Ballesteros, O., Goldsby, D. L., & Kargel, J. S. 2010, SSRv, 153, 273
Durham, W. B., Stern, L. A., & Kirby, S. H. 1996, JGRB, 101, 2989
Duschek, W., Kleinrahm, R., & Wagner, W. 1990, J. Chem. Thermodyn., 22, 841
Edwards, T. J., Newman, J., & Prausnltz, J. M. 1978, Industrial & Engineering Chemistry Fundamentals, 17, 264
Fu, R., O'Connell, R. J., & Sasselov, D. D. 2010, ApJ, 708, 1326
Gasem, K., Gao, W., Pan, Z., & Robinson, R. L. 2001, Fluid Ph. Equilibria, 181, 113
Gattuso, J.-P., & Hansson, L. 2011, Ocean Acidification (Oxford: Oxford Univ. Press)
Gernert, J., & Span, R. 2016, The Journal of Chemical Thermodynamics, 93, 274
Gillon, M., Triaud, A. H. M. J., Demory, B.-O., et al. 2017, Natur, 542, 456
Grimm, S. L., Demory, B.-O., Gillon, M., et al. 2018, A&A, 613, A68
Hirai, H., Komatsu, K., Honda, M., et al. 2010, JChPh, 133, 124511
Hirschmann, M. M. 2016, AmMin, 101, 540
Holden, J. F., & Daniel, R. M. 2010, The Subseafloor Biosphere at Mid-Ocean Ridges (Washington, DC: AGU), 13
Hu, J., Duan, Z., Zhu, C., & Chou, I.-M. 2007, ChGeo, 238, 249
Jäger, A., & Span, R. 2012, J. Chem. Eng. Data, 57, 590
Jäger, A., Vinš, V., Span, R., & Hrubý, J. 2016, Fluid Ph. Equilibria, 429, 55
Kalousová, K., Sotin, C., Choblet, G., Tobie, G., & Grasset, O. 2018, Icar, 299, 133
Kasting, J. F. 1988, Icar, 74, 472
Kasting, J. F. 1991, Icar, 94, 1
Kasting, J. F., & Ackerman, T. P. 1986, Sci, 234, 1383
Kasting, J. F., & Catling, D. 2003, ARA&A, 41, 429
Kasting, J. F., Whitmire, D. P., & Reynolds, R. T. 1993, Icar, 101, 108
Kite, E. S., & Ford, E. B. 2018, ApJ, 864, 75
Kite, E. S., Gao, P., Goldblatt, C., et al. 2017, NatGe, 10, 737
Kite, E. S., Manga, M., & Gaidos, E. 2009, ApJ, 700, 1732
Kitzmann, D., Alibert, Y., Godolt, M., et al. 2015, MNRAS, 452, 3752
Kopparapu, R. K., Ramirez, R. M., SchottelKotte, J., et al. 2014, ApJL, 787, L29
Kopparapu, R. K., Wolf, E. T., Arney, G., et al. 2017, ApJ, 845, 5
Kopparapu, R. K., Ramirez, R., Kasting, J. F., et al. 2013, ApJ, 765, 131
Kuchner, M. J. 2003, ApJL, 596, L105
Kunz, O., Klimeck, R., Wagner, W., & Jaeschke, M. 2007, The GERG-2004 Wide-Range Equation of State for Natural Gases and Other Mixtures, Tech. Rep., GERG Technical Monograph
Kunz, O., & Wagner, W. 2012, J. Chem. Eng. Data, 57, 3032
Léger, A., Selsis, F., Sotin, C., et al. 2004, Icar, 169, 499
Levi, A., & Sasselov, D. 2018, ApJ, 857, 65
Levi, A., Sasselov, D., & Podolak, M. 2013, ApJ, 769, 29
Levi, A., Sasselov, D., & Podolak, M. 2014, ApJ, 792, 125
Levi, A., Sasselov, D., & Podolak, M. 2017, ApJ, 838, 24
Liu, L. G. 1984, E&PSL, 71, 104
Lopez, E. D., Fortney, J. J., & Miller, N. 2012, ApJ, 761, 59
Løvseth, S. W., Austegard, A., Westman, S. F., et al. 2018, Fluid Ph. Equilibria, 466, 48
Luger, R., Barnes, R., Lopez, E., et al. 2015, AsBio, 15, 57
Marshall, J., Ferreira, D., Campin, J.-M., & Enderton, D. 2007, JAtS, 64, 4270
Massani, B., Mitterdorfer, C., & Loerting, T. 2017, JChPh, 147, 134503
Mumma, M. J., & Charnley, S. B. 2011, ARA&A, 49, 471
Nettelmann, N., Fortney, J. J., Kramm, U., & Redmer, R. 2011, ApJ, 733, 2
Noack, L., Höning, D., Rivoldini, A., et al. 2016, Icar, 277, 215
Öberg, K. I., Boogert, A. C. A., Pontoppidan, K. M., et al. 2011, ApJ, 740, 109
Olinger, B. 1982, JChPh, 77, 6255
Ootsubo, T., Kawakita, H., Hamada, S., et al. 2012, ApJ, 752, 15
Pan, D., & Galli, G. 2016, SciA, 2, e1601278
Poirier, J. P. 1982, Natur, 299, 683
Poirier, J. P. 1994, PEPI, 85, 319
Poirier, J. P., Sotin, C., & Peyronneau, J. 1981, Natur, 292, 225
Ramirez, R. M., & Levi, A. 2018, MNRAS, 477, 4627
Raymond, S. N., Quinn, T., & Lunine, J. I. 2004, Icar, 168, 1
Rogers, L. A., Bodenheimer, P., Lissauer, J. J., & Seager, S. 2011, ApJ, 738, 59
Rogers, L. A., & Seager, S. 2010, ApJ, 716, 1208
Saleh, G., & Oganov, A. R. 2016, NatSR, 6, 32486
Selsis, F., Chazelas, B., Bordé, P., et al. 2007, Icar, 191, 453
Sloan, E. D., & Koh, C. 2007, Clathrate Hydrates of Natural Gases (3rd ed.; Boca Raton, FL: CRC Press)
Soave, G. 1972, ChEnS, 27, 1197
Sotin, C., Gillet, P., & Poirier, J. 1985, Ices in the Solar System (Berlin: Springer), 109
Sotin, C., Grasset, O., & Mocquet, A. 2007, Icar, 191, 337
Span, R. 2013, Multiparameter Equations of State: An Accurate Source of Thermodynamic Property Data (Berlin: Springer-Verlag)
Span, R., Eckermann, T., Herrig, S., et al. 2016, TREND. Thermodynamic Reference and Engineering Data
Span, R., & Wagner, W. 1996, JPCRD, 25, 1509
Span, R., & Wagner, W. 1997, IJT, 18, 1415
Spycher, N., Pruess, K., & Ennis-King, J. 2003, GeCoA, 67, 3015
Tobie, G., Lunine, J. I., & Sotin, C. 2006, Natur, 440, 61
Toon, O. B., McKay, C. P., Ackerman, T. P., & Santhanam, K. 1989, JGRD, 94, 16287
Tulk, C. A., Machida, S., Klug, D. D., et al. 2014, JChPh, 141, 174503
Turbet, M., Forget, F., Leconte, J., Charnay, B., & Tobie, G. 2017, E&PSL, 476, 11
Turcotte, D., & Schubert, G. 2014, Geodynamics (Cambridge: Cambridge Univ. Press)
Unterborn, C. T., Desch, S. J., Hinkel, N. R., & Lorenzo, A. 2018a, NatAs, 2, 297
Unterborn, C. T., Hinkel, N. R., & Desch, S. J. 2018b, RNAAS, 2, 116
Van der Waals, J. H., & Platteeuw, J. C. 1959, AdChP, 2, 1
Vinš, V., Jäger, A., Hrubý, J., & Span, R. 2017, Fluid Ph. Equilibria, 435, 104
Vinš, V., Jäger, A., Span, R., & Hrubý, J. 2016, Fluid Ph. Equilibria, 427, 268
von Paris, P., Grenfell, J. L., Hedelt, P., et al. 2013, A&A, 549, A94
Wagner, W., & Pruß, A. 2002, JPCRD, 31, 387
Walker, J., Hays, P. B., & Kasting, J. F. 1981, JGRC, 86, 9776
Wang, H., Zeuschner, J., Eremets, M., Troyan, I., & Willams, J. 2016, Natur, 6, 19902
Wendland, M., Hasse, H., & Maurer, G. 1999, J. Chem. Eng. Data, 44, 901
Wiryana, S., Slutsky, L. J., & Brown, J. M. 1998, E&PSL, 163, 123
Yang, J., Cowan, N. B., & Abbot, D. S. 2013, MNRAS, 771, L45